

Decihertz gravitational waves from double white dwarf merger remnants

SHIN'ICHIROU YOSHIDA¹

¹*Department of Earth Science and Astronomy*

Graduate School of Arts and Sciences, The University of Tokyo

Komaba 3-8-1, Meguro-ku, Tokyo 153-8902, Japan

(Received; Revised; Accepted)

Submitted to ApJ

ABSTRACT

Close binaries of double white dwarfs (DWDs) inspiral and merge by emitting gravitational wave (GW). Orbital motion of some of these binaries are expected to be observed at low frequency band by space-borne laser interferometric detectors of GW. The merger remnant may suffer thermonuclear runaway and explode as type Ia supernova if they are massive enough. As GW sources the remnants have so far been scarcely studied. Here we propose a new mechanism of GW emission from DWD merger remnants which may be observed by planned GW detectors in decihertz frequency band. A remnant is temporarily expected to have a high degree of differential rotation as a consequence of merger process. It is then unstable to oscillation modes whose azimuthal pattern speed coincides with the stellar rotation. We solve eigenvalue problem of differentially rotating remnants and identify unstable eigenmodes which may be categorized to inertial modes. The estimate of characteristic strain of GW shows that they may be detectable

within the distance of the Virgo cluster by planned gravitational wave observatories targeting the decihertz band.

Keywords: white dwarfs — binary stars — gravitational wave sources

1. INTRODUCTION

Close binary systems composed of two white dwarfs, double white dwarf (DWD) binaries, emit gravitational wave and may merge within the age of the Universe. The gravitational wave from those inspiraling binaries are expected to be seen (not necessarily welcomed, though, since it may be a hindrance to observe other sources) by the proposed space-borne laser interferometric gravitational observatory such as Laser Interferometer Space Antenna (LISA, [Amaro-Seoane et al. \(2012\)](#)) or Tian-Qin ([Luo et al. 2016](#); [Huang et al. 2020](#)). The outcomes of the mergers may depend on the masses of the progenitor binaries. One of the most interesting possibility is the merger of a binary whose total mass is close to or exceed the Chandrasekhar mass may lead to type Ia supernovae (SNIa) of thermonuclear origin ([Webbink 1984](#); [Iben & Tutukov 1984](#)). The systems with the smaller total mass may survive the nuclear runaway after the merger and may leave R Coronae Borealis stars ([Webbink 1984](#)) or massive/strongly magnetized white dwarfs ([Ferrario et al. 2015](#)). The event rate for these mergers are crudely estimated as follows. Taking the merger rate R_{merge} of double white dwarfs population in the Galactic disk to be $(6.3 \pm 1.0) \times 10^{-13} \text{yr}^{-1} M_{\odot}^{-1}$ ([Maoz et al. 2018](#)) and extrapolated number density n of Milky Way type galaxy to be $(1 - 1.5) \times 10^{-2} \text{Mpc}^{-3}$ ([Kalogera et al. 2001](#)), we have the merger rate \mathcal{R} of double white dwarf binary up to the distance D as,

$$\mathcal{R}(D) \sim \frac{4\pi}{3} D^3 R_{\text{merge}} \cdot n \cdot M_{\text{disk}} \sim 14 \left(\frac{D}{20 \text{Mpc}} \right)^3 \text{yr}^{-1} \quad (1)$$

Here Milky Way's disk mass M_{disk} is taken from [Licquia & Newman \(2015\)](#). Notice that this rate takes into account neither the halo/bulge of disk galaxies nor the contribution from elliptical or dwarf galaxies. ¹

¹ [Huang et al. \(2020\)](#) estimates the rate of inspiraling DWD with the total mass larger than $2M_{\odot}$ in the Local Group of galaxies. Their event rate is smaller than obtained here, since the masses of the components are higher and the volume observed is smaller than are considered here.

According to the hydrodynamical simulations of the merger, the less massive secondary star fills its Roche lobe before the stars contact and the dynamical accretion of tidally disrupted secondary onto the massive primary star occurs (Benz et al. 1990; Segretain et al. 1997; Lorén-Aguilar et al. 2005, 2009; Yoon et al. 2007a; Dan et al. 2011, 2012; Pakmor et al. 2012; Raskin et al. 2012; Tanikawa et al. 2015; Sato et al. 2015, 2016). Then after the dynamical timescale the remnant settles into a rapidly and differentially rotating quasi-equilibrium state. It may evolve towards the shear-free state in a viscous timescale of typically $10^3 - 10^4$ s (Shen et al. 2012). In this paper we are interested in this quasi-equilibrium transient state of remnant, especially in the outcome of the large degree of differential rotation.

Rotating stars are known to suffer a variety of instabilities which are driven by different physical mechanisms. An instability driven by such dissipative mechanism as viscosity, thermal transport or gravitational radiation is referred to as secular instability, for which the timescale is determined by the characteristic time of the particular dissipation mechanism (Tassoul 1978b). Usually the timescale is longer than the hydrodynamical one. Another category of instability, i.e., dynamical instability, has a purely hydrodynamic origin and the growth time is the hydrodynamical timescale of the system under consideration. Classical studies of self-gravitating homogenous spheroids/ellipsoids revealed that a spheroidal configuration is susceptible to a dynamical instability for $m = 2$ perturbation (m is the azimuthal wave number) when it rotates above a critical speed. The rotation is conventionally parametrized by T/W value, where T and W are rotational kinetic energy and gravitational binding energy of a star respectively. The instability (bar-mode instability) sets in at $T/W \sim 0.27$ (Chandrasekhar 1987; Tassoul & Ostriker 1968; Ostriker & Tassoul 1969; Ostriker & Bodenheimer 1973; Tassoul 1978b). The mechanism of it is explained as two particular oscillation modes merging into a pair of complex conjugate ones (Schutz 1980).

Relatively recently by numerical simulations rotating stars with large degree of differential rotation have been found to suffer another dynamical instability (Pickett et al. 1996; Centrella et al. 2001; Shibata et al. 2002, 2003; Saijo et al. 2003; Ou & Tohline 2006; Corvino et al. 2010). The instability is characterized by significantly lower threshold value of T/W parameter than that of classical bar-

mode, which may be as low as $\mathcal{O}[10^{-2}]$. The mechanism of the instability has been explained as a corotation of wave pattern of unstable eigenmode with the stellar rotation (Watts et al. 2005; Saijo & Yoshida 2006; Passamonti & Andersson 2015; Saijo & Yoshida 2016; Yoshida & Saijo 2017), which explains why the instability appears in rotating stars with large degree of differential rotation.

Though the saturation amplitude of the instability seen in hydrodynamical simulations is smaller than that of the classical bar-mode, it persists for hundreds of rotation periods without being disrupted by non-linear hydrodynamic effects (Shibata et al. 2002; Saijo & Yoshida 2006). This characteristics of the instability is advantageous for detection of gravitational wave from it, once a compact star is susceptible to the instability.

In this paper linear eigenmode analysis is done for remnant models of binary white dwarf mergers in the early stage of their evolution. Unstable eigenmodes are obtained for various mass, temperature and rotational parameter. The sequence of the fastest growing eigenmodes seems to share common characteristics for all the models considered here. Moreover the gravitational wave strain from the unstable oscillations are computed. We discuss the possibility of observing these gravitational wave transients by the proposed detectors in $\mathcal{O}[10^{-2}] - \mathcal{O}[10^{-1}]$ Hz range.

2. FORMULATION

2.1. Equation of state

As for the equation of states of dense matter at finite temperature, we use a simple model of partially degenerate electrons with radiation. The number density of electrons n_e with chemical potential μ and temperature T is written as (Cox & Giuli 1968),

$$n_e = \frac{8\pi\sqrt{2}}{h^3} (m_e c)^3 \theta^{3/2} (F_{1/2}(\eta, \theta) + \theta F_{3/2}(\eta, \theta)), \quad (2)$$

where $\eta \equiv \mu/m_e c^2$ and $\theta \equiv k_B T/m_e c^2$ are a degeneracy parameter and a normalized temperature. Here h, m_e, c, k_B are the Planck's constant, the mass of electron, the speed of light in vacuum and Boltzmann constant. The functions $F_k(\eta, \theta)$ are Fermi-Dirac integrals defined as,

$$F_k(\eta, \theta) = \int_0^\infty \frac{x^k \left(1 + \frac{\theta}{2}x\right)^{1/2}}{1 + e^{x-\eta}} dx \quad (3)$$

where k is the order of the integrals.² Mass density of the gas ρ is written as,

$$\rho = \left[\frac{A}{Z} \right] m_H n_e, \quad (4)$$

where m_H is the atomic mass unit. $\left[\frac{A}{Z} \right]$ is the mean ratio of atomic mass number A to atomic number Z . Here we assume it to be two for simplicity. Electron pressure p_e is expressed as

$$p_e = \frac{16\pi\sqrt{2}m_e^4c^5}{3h^3}\theta^{5/2} \left(F_{3/2}(\eta, \theta) + \frac{\theta}{2}F_{5/2}(\eta, \theta) \right). \quad (5)$$

Internal energy density u_e is similarly written as

$$u_e = \frac{8\pi\sqrt{2}m_e^4c^5}{3h^3}\theta^{5/2} \left(F_{3/2}(\eta, \theta) + \theta F_{5/2}(\eta, \theta) \right). \quad (6)$$

Then the entropy of gas per mass s_e is,

$$s_e = \frac{u_e + p_e}{\rho T} - \frac{\eta n_e k_B}{\rho}. \quad (7)$$

We assume a simple isentropic model of a remnant, for which the specific entropy s_e is kept constant in it. Then the adiabatic exponent Γ which is necessary for the linear perturbation analysis is computed as follows. Varying s_e and set it zero, we have a linear adiabatic relation between $\Delta\eta$ and $\Delta\theta$ where Δ mean small variations of η and θ , This relation is used to evaluate adiabatic exponent of the gas Γ_e ,

$$\Gamma_e \equiv \frac{\Delta \ln p_e(\Delta\eta, \Delta\theta)}{\Delta \ln \rho(\Delta\eta, \Delta\theta)}. \quad (8)$$

Photon's radiation pressure p_γ is added to p_e to produce the total pressure,

$$p_\gamma = \frac{a}{3}T^4, \quad (9)$$

where a is the radiation density constant.

The total adiabatic exponent Γ is then given by (Tassoul 1978a)

$$\Gamma = \beta_e + \frac{(\Gamma_e - 1)(4 - 3\beta_e)}{\beta_e + 12(\Gamma_e - 1)(1 - \beta_e)}, \quad (10)$$

where $\beta_e = p_e/(p_e + p_\gamma)$. As is easily seen, $\Gamma \rightarrow 4/3$ as $\beta_e \rightarrow 0$.

² We compute the Fermi-Dirac integrals by using publicly available code sets from http://cococubed.asu.edu/code_pages/fermi_dirac.shtml.

2.2. Equilibrium models

To compute the remnant models, we assume them to be in dynamical equilibrium with axisymmetry. Isentropic nature of the configuration makes it possible to apply Hachisu's self-consistent field method (Hachisu 1986). With a prescribed angular frequency profile $\Omega = \Omega(r \sin \theta)$, where r and θ are the polar radial and angular coordinates, we may compute equilibrium models of rotating stars up to mass-shedding limit.³ Rotational deformation is conventionally measured by the axis ratio parameter r_p/r_e where r_p and r_e are the polar and the equatorial radius of the model.

As for the rotational profile we adopt the differential rotation law in Yoshida (2019), especially called 'Yoon07' there, which analytically fit the rotational profile of a merger simulation in Yoon et al. (2007b). The profile has a slowly and uniformly rotating core and a nearly Keplerian envelope. The explicit expression is

$$\frac{\Omega(R)}{\Omega_c} = \beta \left(\left(1 + \left(\frac{R}{R_c} \right)^{3/2} \right)^{-1} (1 + e^{-\alpha x})^{-1} - (1 + e^{\alpha})^{-1} \right) + 1; \quad x \equiv 2r^B - 1, \quad B = \frac{\ln \frac{1}{2}}{\ln R_c} \quad (11)$$

The profile depends on four parameters, $\Omega_c, R_c, \alpha, \beta$. They are respectively, the angular frequency at the origin, the radius of the uniformly rotating core normalized by the equatorial radius of the star, the parameter controlling the steepness of the Ω increment above the core, and the parameter controlling the maximum ratio of Ω to Ω_c . In Fig.1 we show typical angular frequency profiles for different sets of the parameters. Notice that Ω above the core asymptotes to the Keplerian distribution $\Omega \propto R^{-3/2}$.

We fix the temperature and the density at the center to compute the specific entropy of the models. The thermodynamic quantities in the stellar interior are computed by assuming constancy of the entropy.

2.3. Perturbations

In this study we perform linear perturbation analysis of the remnant models. The formulation and the numerical code are based on Saijo & Yoshida (2006); Yoshida & Saijo (2017) where the equilib-

³ By Poincaré-Wavre theorem, the angular frequency depends only on the distance from the rotational axis (Tassoul 1978a)

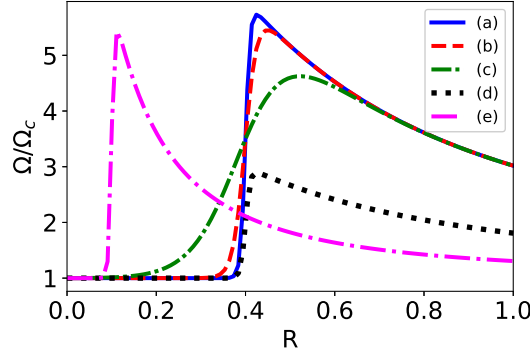


Figure 1. Profiles of angular velocity. The radial coordinate R is normalized by the equatorial radius. The angular frequency Ω is normalized by the value at the origin Ω_c . (a) $(\alpha, \beta, R_c) = (100, 10, 0.4)$. (b) $(\alpha, \beta, R_c) = (40, 10, 0.4)$. (c) $(\alpha, \beta, R_c) = (10, 1, 0.4)$. (d) $(\alpha, \beta, R_c) = (100, 4, 0.4)$. (e) $(\alpha, \beta, R_c) = (100, 10, 0.1)$.

rium star is approximated as a flattened configuration. Then we solve a set of ordinary differential equations of radial coordinate. This approximation is to make the problem largely simplified. Otherwise we would need to solve the two-dimensional eigenvalue problem whose computational domain is the meridional section of a star. This is rather hard a problem especially when we have corotation radii at which the stellar rotation coincides with the azimuthal pattern speed of an eigenmode (see Eq.(13) and the comment below the equation). We may justify the formulation if the eigenmodes here share the same characteristics as the eigenmodels susceptible to the low T/W instability. In Saijo & Yoshida (2006) we found the characteristics of low-T/W instability using three-dimensional hydrodynamical simulations. The panel II of Fig.5 in Saijo & Yoshida (2006) shows the characteristic velocity pattern of low T/W instability seen in the simulation. It is noticed that the velocity perturbation lacks the component parallel to the rotational axis anywhere except at the surface. This planar velocity perturbation means that the dimensionless density perturbation also has a planar profile perpendicular to the axis. Then the perturbation is quasi-planar and the equations may be well-approximated by the radial ordinary differential equations when the azimuthal dependence is decomposed into harmonics. Checking the validity of the approximation is beyond our scope here. Thus the results shown below are presented to show a 'proof of principle' and should not to be taken as the detailed results for realistic remnants.

Our "cylindrical model" deals with a system of equation only in the equatorial plane and neglect the z -dependence of the perturbed variables. We utilize the two potential formalism of [Ipser & Lindblom \(1991\)](#). The linear adiabatic perturbation equations for a stationary and axisymmetric fluid configuration are cast into a coupled system of two scalar potentials; $\delta\Phi$, the perturbed gravitational potential and δU , the sum of the perturbed enthalpy and the gravitational potential. Both of the potentials are defined in the Eulerian description of fluid. In cylindrical coordinate (R, φ, z) we have two equations of the potentials as

$$\begin{aligned}
0 = & \frac{d^2}{dR^2} \delta U \\
& + \left[\partial_R \ln \left(\frac{s}{L} \right) - \frac{2m\Omega}{sR} + \frac{1}{R} + \frac{\partial_R \rho}{\rho} + \frac{m\kappa^2}{2\Omega s R} \right] \frac{d}{dR} \delta U \\
& + \left[-\frac{L}{s} \partial_R \left(\frac{2m\Omega}{RL} \right) + \frac{L}{c_s^2} - \frac{2m\Omega}{sR} \left(\frac{1}{R} + \frac{\partial_R \rho}{\rho} \right) - \frac{m^2}{R^2} \right] \delta U \\
& - \frac{L}{c_s^2} \delta \Phi,
\end{aligned} \tag{12}$$

and

$$\left(\frac{d^2}{dR^2} + \frac{1}{R} \frac{d}{dR} - \frac{m^2}{R^2} \right) \delta \Phi = 4\pi\rho \left(\frac{d\rho}{dp} \right) (\delta U - \delta \Phi), \tag{13}$$

where we assume harmonic dependence of Eulerian perturbations on t and φ as $\sim e^{-i\sigma t + im\varphi}$. Here ρ is the equilibrium density, Ω is the angular velocity of equilibrium flow, $\kappa^2 = 2\Omega(2\Omega + R\partial_R\Omega)$ is the epicyclic frequency squared, $s = \sigma - m\Omega$ is the frequency seen from a co-moving observer to the equilibrium flow, $L = s^2 - \kappa^2$ and the sound speed of equilibrium fluid is c_s . We call the zero of s as a corotation singularity, which is a simple pole of equation (12) in the complex R -plane. In the former studies [Saijo & Yoshida \(2006\)](#); [Yoshida & Saijo \(2017\)](#) we assume the imaginary part of σ is much smaller than the real part. Then the zero of s is regarded to locate on the real R -axis. The path bypassing the zero in the complex R -plane leads to the small imaginary part of the eigenfrequency. In this work we do not assume the imaginary part to be much smaller than the real part, thus the integration path of the perturbation equation on the real R -axis do not have a singularity.

The search for an eigenvalue is done as follows. For a given complex number σ , we numerically integrate the equations from the center and the surface of the star. The boundary conditions imposed

are the same as in Saijo & Yoshida (2006); Yoshida & Saijo (2017), i.e., the regularity at the center and the free surface condition as well as the regularity of the gravitational potential at the infinity. At a matching point inside the star we compute the Wronskian of the solutions. The zeroes of the Wronskian are eigenvalues and we search for them by using Muller's method (Press et al. 1992) in the complex σ -plane.

2.4. Gravitational wave

2.4.1. Quadrupole formula

To compute the gravitational wave amplitude we adopt the quadrupole formula of the metric function for fluid systems (Oohara & Nakamura 1989; Blanchet et al. 1990; Zwerger & Müller 1997). Transvers-Traceless (TT) component h_{ij}^{TT} of the spatial part of the metric perturbation (by which full metric is written as $\eta_{\mu\nu} + h_{\mu\nu}$ with $\eta_{\mu\nu} = \text{diag}(-1, 1, 1, 1)$) is⁴

$$h_{ij}^{TT} = \frac{2G}{c^4 D} \mathbf{P}_{ijkl} \int d^3 \vec{x} \rho [2v^k v^l - x^k \partial^\ell \Phi - x^\ell \partial^k \Phi], \quad (14)$$

where ρ , v^k , Φ , D are mass density, velocity of fluid, gravitational potential, and the distance to the source. Here the cartesian coordinate is used whose origin is at the center of mass of the gravitational wave source. Notice that $\partial^k = \partial_k$ for the cartesian coordinate. \mathbf{P} is the projection tensor perpendicular to the line of sight to the source,

$$\mathbf{P}_{ijkl} = \gamma_{ik} \gamma_{jl} - \frac{1}{2} \gamma_{ij} \gamma_{kl}, \quad ; \gamma_{ij} \equiv \delta_{ij} - N_i N_j \quad (15)$$

where δ_{ij} is the unit tensor and N_i is the directional unit vector pointing towards the observer from the origin. The viewing angle is expressed by N_i which we choose to coincide with the unit vector parallel to the rotational axis of the star (i.e., z-direction) for simplicity.

We here focus on the quadrupole mode of stellar oscillation with the azimuthal wave number $m = 2$, thus the eigenfunctions linearly enter to Eq.(14).

It should be remarked that the spatial integration in Eq.(14) is performed by assuming the planar behavior perpendicular to the rotational axis, as is remarked in Sec.2.3.

⁴ Here Latin indices are for spatial coordinates, while Greek ones are for spacetime coordinates.

2.4.2. Characteristic strain

For such a gravitational wave source with a secularly changing frequency as an inspiraling compact binary, the characteristic strain h_c is the conventional signal parameterization of gravitational wave (see e.g., [Moore et al. \(2015\)](#)). It is related to the number of cycles N_c for which the oscillations of gravitational wave strain with a given frequency lasts,

$$h_c = \sqrt{N_c} h_0, \quad (16)$$

where h_0 is the amplitude of nearly sinusoidal gravitational wave strain.

Eigenfrequencies of a merger remnant changes as it secularly evolves in a secular time scale longer than the dynamical one. The viscous timescale is the second shortest among the relevant timescales, i.e., dynamical, viscous, and thermal. It is the one during which the rotational profile of the remnant changes and the change affects the eigenfrequency. The viscous timescale is estimated for two cases in [Shen et al. \(2012\)](#). One of them assumes the α -viscosity ([Shakura & Sunyaev 1973](#)) resulting from magneto-rotational turbulence. The order of timescale is 10^4 sec. It should, however, be noticed that the criterion of the magneto-rotational instability ([Velikhov 1959](#); [Chandrasekhar 1960](#); [Balbus & Hawley 1991](#)) is not satisfied at the core-envelope boundary, where $d\Omega/dr > 0$. The other one comes from Tayler-Spruit dynamo ([Tayler 1973](#); [Spruit 1999, 2002](#); [Piro 2008](#)), which results in the timescale of 10^4 seconds for our typical rotational profile ((a) in Fig.1). For the estimate above, we use Eq.(1) and Eq.(5) in [Shen et al. \(2012\)](#). Overall the viscous timescale in which differential rotation of remnants is smoothed out may be 10^4 s. The duration of saturated oscillations is expected to be shorter than this timescale, since it takes e-folding time for a unstable mode to saturate. This e-folding time is typically less than 10^2 s for the fastest growing eigenmodes. I choose the typical duration of saturated oscillation to be 10^3 s. Thus the number of cycles of the initially unstable oscillation with frequency f is at most $N_c = f\tau_0$. Here we fix τ_0 to be 10^3 s for simplicity and compute the characteristic strain by Eq.(16).

2.4.3. Fixing amplitude of the eigenmodes

To estimate gravitational wave amplitude of eigenmode oscillations of stars, we need to specify the amplitude of the eigenmode functions. This is not in principle done within the linear theory, for which the amplitude is 'small' but arbitrary. We thus parametrize the amplitude of the modes. Shibata et al. (2002) studied $N = 1$ polytrope with differential rotation by using nonlinear hydrodynamical simulations and found that the low T/W dynamical instability has an amplitude of $\mathcal{O}[10^{-2} \sim 10^{-1}]$ measured by a distortion parameter $\eta = |I_{xx} - I_{yy}|/(I_{xx} + I_{yy})$ where I_{ij} are instantaneous moments of inertia. While Lovelace et al. (2009) and Meheut et al. (2013) argued that the Rossby-wave instability in astrophysical disks may be saturated at the amplitude of velocity perturbation for which the circulation time of the local vortex is comparable to the growth time of the instability.

We here introduce the ellipticity ϵ_I of the deformed star due to the eigenmode as

$$\epsilon_I = \left| \frac{\delta I_{zz}}{I_{zz}} \right| = \left| \frac{\int dV \delta \rho R^4}{\int dV \rho R^4} \right|. \quad (17)$$

The amplitude of the eigenmode scales linearly as ϵ_I . As the parameter may be a proxy of the deformation parameter η in Shibata et al. (2002), we may set $\epsilon_I \sim \mathcal{O}[10^{-2} - 10^{-1}]$. On the other hand when we apply the estimate of saturation amplitude of the Rossby-wave instability, we obtain the amplitude of $\mathcal{O}[10^{-5}]$. Therefore we here fix the range of the amplitude parameter to be $10^{-5} \leq \epsilon_I \leq 10^{-1}$.

3. RESULTS

We here focus our attention to $m = 2$ modes which are expected to be the most important oscillations that couple to gravitational wave.⁵

3.1. Unstable eigenmodes

In Fig.2 we plot eigenfrequency and equilibrium variables as functions of axis ratio, which measures the rotational deformation of equilibria. Panels of (a) are for $R_c = 0.4$, while those of (b) are

⁵ $m = 1$ modes may be excited in a merger remnant (Kashyap et al. 2017), but the coupling to gravitational wave is at the second order in small perturbation in the quadrupole formula. Higher order than $m = 2$ generally contributes to gravitational radiation with smaller amplitude.

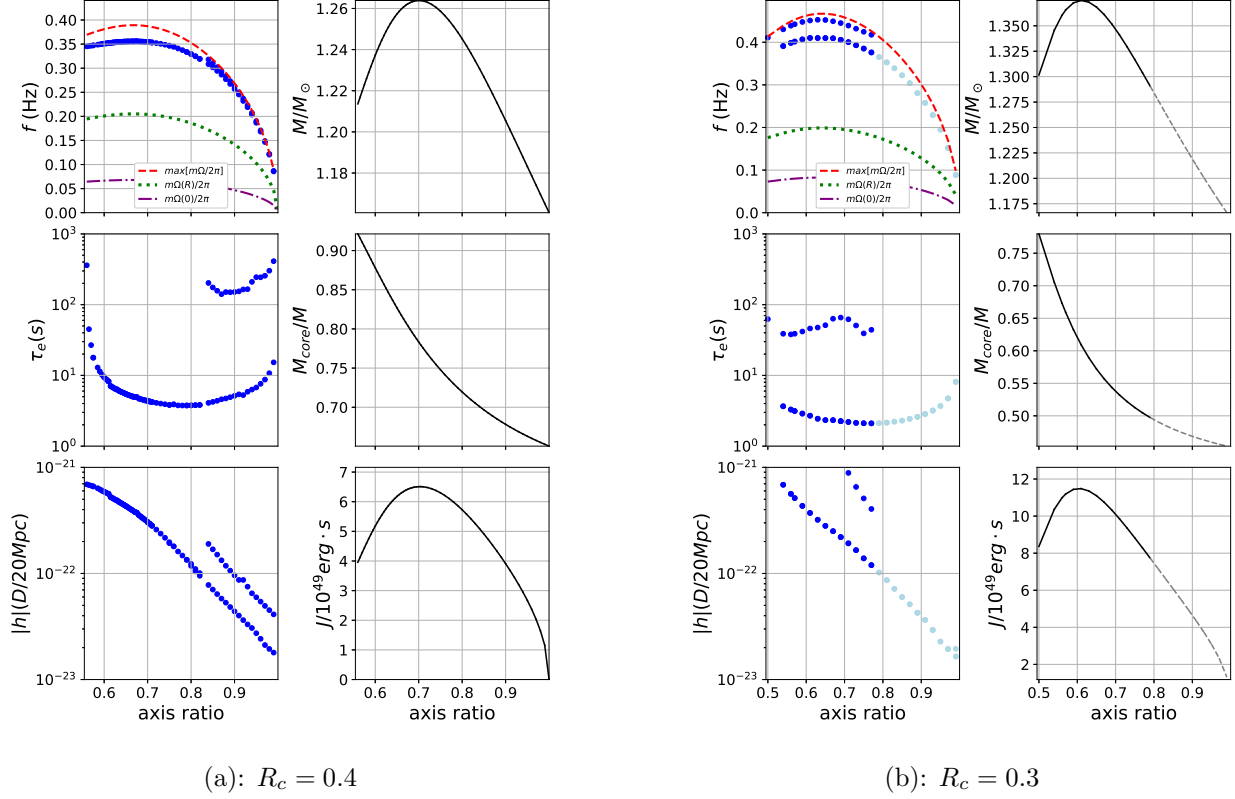


Figure 2. Sequences of eigenmodes and corresponding equilibrium models. Common parameters in both panels are $(T_c \text{ (K)}, \rho_c \text{ (gcm}^{-3}), \alpha, \beta) = (10^7, 10^8, 100, 10)$. The panels (a) are for $R_c = 0.4$ while those of (b) are for $R_c = 0.3$. Top left: Real part of eigenfrequency $\Re[\sigma/2\pi]$ in Hz. Blue dots correspond to the eigenfrequency while the solid curve is the maximum of the corotation frequency. The dotted and the dot-dashed curve are the corotation frequency at the equatorial surface and at the origin, respectively. Middle left: Growth time $\tau_e = \Im[\sigma]^{-1}$ of the eigenmodes. Bottom left: dimensionless strain h of gravitational wave times the source distance D in unit of 20Mpc. Amplitude parameter $\epsilon_I = 10^{-2}$. Top right: Total mass of the equilibrium remnant. Middle right: Mass fraction of the core. Bottom right: Total angular momentum in units of 10^{49} erg s . The leftmost point corresponds to the mass-shedding limit. In the panels (b) Thin dots and the dashed lines correspond to the models whose mass fraction of the core is less than 0.5.

for $R_c = 0.3$. Other parameters are the same for both models, i.e., $(T_c \text{ (K)}, \rho_c \text{ (gcm}^{-3}), \alpha, \beta) = (10^7, 10^8, 100, 10)$. Notice that the smaller axis ratio corresponds to the larger deformation of the star from the sphere (when the axis ratio is unity). First of all we need to be careful to interpret the equilibria as the sequence parametrized by 'speed of rotation'. As the axis ratio decreases from unity the equilibrium suffer the large degree of centrifugal distortion. Along with it the angular momentum

increases when the axis ratio is close to unity. However it is not a monotonic function of the axis ratio. This results from the highly non-monotonic distribution of the angular velocity (see Fig.1). It also follows that the total mass is not monotonic as is seen in the top right panel.

In both panels (a) and (b), the sequence of the real part of eigenfrequency ($\Re[\sigma/2\pi]$) is plotted in the top left panel (blue dots). The red solid curve is the maximum of the corotation frequency inside the star, $\max[m\Omega(R)/2\pi]$. For these equilibrium sequences two discrete sequence of unstable eigenmodes are specified. Both of the mode are within the corotation resonance of frequency, $m\Omega(0) \leq \Re[\sigma] \leq \max[m\Omega]$. For $R_c = 0.4$ case (panel (a)) frequencies of these modes asymptote to zero. One of the mode is unstable all the way through the mass-shedding limit. This mode is the fastest growing mode. The other mode seem to exit from the corotation resonance and be stabilized around the axis ratio of 0.83. The sequence of these modes, whose limiting frequency for non-rotating star (axis ratio being unity) is zero, suggest that they are inertial type of oscillations whose main restoring force is Coriolis force, rather than acoustic type. [Passamonti & Andersson \(2020\)](#) recently reported that remnant models of binary neutron star merger exhibit low T/W instability (see also [Xie et al. \(2020\)](#)). They find there are two types of unstable modes, which corresponds to acoustic type (f-mode) and the rotationally supported inertial mode (i-mode). Although their functional form of the profile of the rotational angular frequency is different from ours, they share a qualitative similarity, that is, nearly flat profile around the origin and the off-center maximum of Ω . It should be noted that the frequency of the unstable modes is close to the maxima of corotaion frequency. We find no unstable modes whose corotation point is either close to the origin or to the stellar surface. Remarkably in the current study the fastest growing modes of equilibrium stars for the other parameter sets share the same inertial type of nature.

For the case with $R_c = 0.3$ (b) we see the equilibrium model may have the core fraction less than 0.5. Our assumption on the remnant is that the secondary of the progenitor binary is disrupted and accreted onto the primary, which forms the envelope of the remnant while the core consists of the matter in the primary. As a result the core mass should be larger than the envelope mass. We therefore discard the portion of the sequence with the mass fraction being less than 0.5. For the

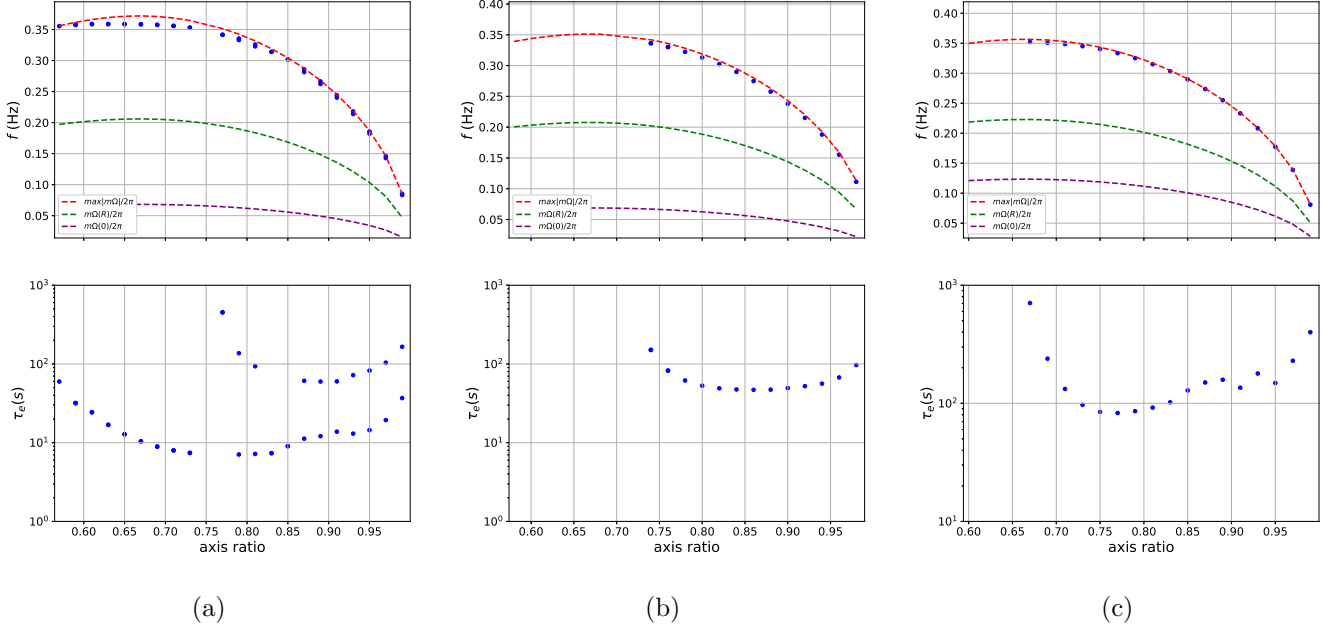


Figure 3. (a) Eigenfrequency $\Re[\sigma/2\pi]$ (top panel) and growth time $\tau_e = \Im[\sigma]^{-1}$ for $(T_c, \rho_c, \alpha, \beta, R_c) = (10^7, 10^8, 40, 10, 0.4)$. (b) $(T_c, \rho_c, \alpha, \beta, R_c) = (10^7, 10^8, 20, 10, 0.4)$. (c) $(T_c, \rho_c, \alpha, \beta, R_c) = (10^7, 10^8, 100, 4, 0.4)$.

sequence in (b) the models with the axis ratio less than 0.78 is the allowed models. We see the fastest growing mode has the characteristics of the inertial mode (see the top left). The other less unstable mode seems to have a different character. As the axis ratio decreases from unity (the degree of rotational deformation increases), the mode which is initially outside the corotation band (below the red dashed curve of the top left panel) seems to enter the corotation band and becomes unstable. The mode seems not to asymptote to the zero frequency mode and may have an acoustic nature.

(c) is the model with smaller β than in Fig.2. β is a measure of the maximum Ω as is seen in Fig.1. For the value of $\beta \lesssim 2$, we find no unstable mode.

Fig.3 is compared with the top and middle left panels of Fig.2. (a) and (b) correspond to the smaller α models, for which the gradient of Ω at the core-envelope interface are smaller (see Fig.1). When the gradient of Ω becomes too small (when $\alpha \lesssim 10$) we find no unstable eigenmode. Notice that this variation of α modifies very little such bulk quantities as the total mass, core mass fraction, and the angular momentum.

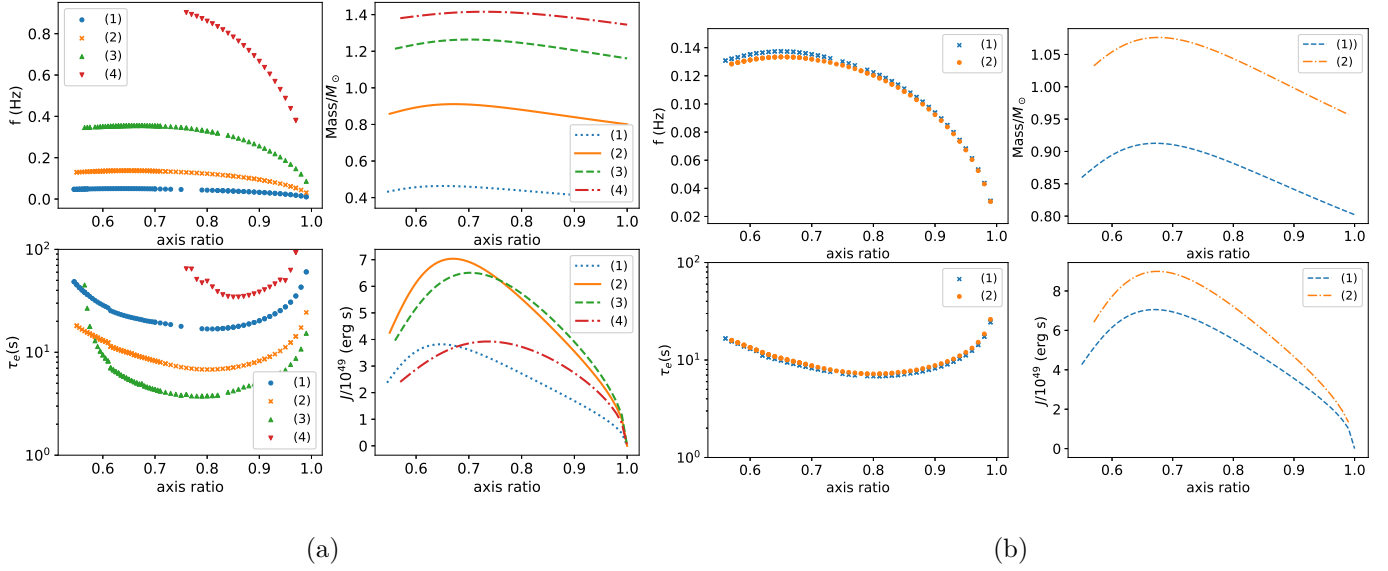


Figure 4. Eigenfrequency $\Re[\sigma/2\pi]$ (top left), growth time $\tau_e = \Im[\sigma]^{-1}$ (bottom left), mass in M_\odot (top right), and angular momentum in 10^{49} erg s. In the panels (a), the temperature T_c is fixed to be 10^7 K and the central density ρ_c is varied. (1): $\rho_c = 10^6$ gcm $^{-3}$, (2): $\rho_c = 10^7$ gcm $^{-3}$, (3): $\rho_c = 10^8$ gcm $^{-3}$, (4): $\rho_c = 10^9$ gcm $^{-3}$. In the panels (b), ρ_c is fixed to be 10^7 gcm $^{-3}$, while T_c is varied. (1): $T_c = 10^8$ K, (2): $T_c = 10^9$ K.

In Fig.4 we compare the equilibria and the eigenmodes for different ρ_c (panels (a)) and for different T_c (panel (b)). R_c, α, β are fixed. The unstable modes are of the inertial type. The eigenfrequency of the modes is higher for the higher ρ_c (thus massive) models. The growth time is not a monotonic function of the density or the mass. rather It may be correlated with the angular momentum of the star (the bottom right of (a)). The model with higher angular momentum seems to have the smaller growth time.

In the panels (b) we plot the eigenfrequency, the growth rate as well as the mass and the angular momentum for different value of T_c . The model (2) with $T_c = 10^9$ K correspond to the higher temperature and the mass is larger due to the support of the thermal pressure as well as the degenerate electron pressure. The model (1) has $T_c = 10^8$ K for which thermal pressure makes small difference from the lower temperature models. Only weak dependence on T_c is seen both in the frequency and the growth time, at least as high as $T_c \sim 10^9$ K.

3.2. Characteristic strain of gravitational wave from unstable modes

One of the most interesting questions on the oscillations of the merger remnants is whether they are observable by some of the planned detectors of gravitational waves. Since the typical frequency of the remnants are in the deci-Hz range, they are neither good targets for the now-operating interferometers such as Laser Interferometer Gravitational-wave Observatory (LIGO, <https://www.ligo.org/>), Virgo (<https://www.virgo-gw.eu/>), and KAGRA (<https://gwcenter.icrr.u-tokyo.ac.jp/en/>), nor planned LISA, the space-borne gravitational wave detector for low-frequency range. The deci-Hz range gravitational wave detections are currently planned with different technologies, because of such astrophysical/cosmological interests as discovery of intermediate-mass black holes, cosmological background gravitational waves, precise measurements of neutron stars/black holes binary characteristics (Sedda et al. 2019). One type of detectors is the space-borne antennae system similar to LISA but with shorter baselines, i.e., Big Bang Observer (BBO, Crowder & Cornish (2005)), DECi-hertz Interferometer Gravitational-wave Observatory (DECIGO, Kawamura et al. (2006)), and TianQin (Luo et al. 2016). Other types of detectors proposed are TOrsion Bar Antennae (TOBA, Ando et al. (2010)) and atomic interferometers (Graham et al. 2017; Badurina et al. 2020; Abou El-Neaj et al. 2019).

For simplicity we compute the characteristic strain of gravitational wave from dynamically unstable remnants by assuming the following conditions. First we assume only the fastest growing mode contributes the strain. Secondly the saturated mode keeps its frequency and amplitude for viscous timescale τ_0 (see Sec.2.4.2) and diminishes. Inclusion of the multiple unstable modes and the evolution of eigenmodes as the remnant evolves in viscous timescale is beyond our scope here.

In Fig.5 the sequences of characteristic strain h_c for the fastest growing mode in $(T, \rho_c, \alpha, \beta, R_c) = (10^8 \text{K}, 10^8 \text{g cm}^{-3}, 100, 10, 0.4)$ stars are plotted. For all models here the fastest growing mode is of inertial nature. Therefore the non-rotating limit is not in the plots, since the eigenfrequency vanishes. The (black) triangles pointing downward are h_c for which the maximal amplitude of $\epsilon_I = 0.1$ are assumed following Shibata et al. (2002). The (red) triangles pointing upward correspond to the minimal amplitude estimated in the same way as Rossby-wave instability (Meheut et al. 2013),

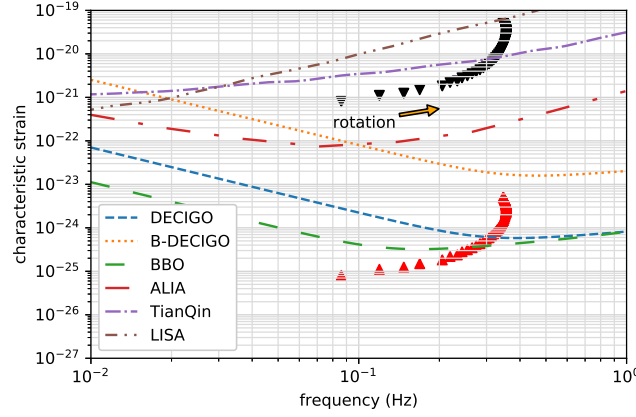


Figure 5. Characteristic strain of gravitational wave from the fastest growing eigenmodes for $T = 10^8\text{K}$, $\rho_c = 10^8\text{g cm}^{-3}$, $\alpha = 100$, $\beta = 10$, and $R_c = 0.4$. The (black) triangles pointing downward correspond to the case with the saturation amplitude (ϵ_I) being 10^{-1} , while the (red) triangles pointing upward correspond to the case with $\epsilon_I = 10^{-5}$. Distance to the source is assumed to be 20Mpc. Along the sequence, the direction of the faster rotation (measured by the axis ratio) is indicated by an arrow. Also plotted are sensitivity curves for DECIGO (dashed), B-DECIGO (dotted), BBO (long-dashed), ALIA (long-dash-dotted), TianQin (dash-dotted), and LISA (dash-double-dotted). Data of these sensitivity curves are taken from <http://gwplotter.com> except for DECIGO, B-DECIGO, and BBO.

$\epsilon_I = 10^{-5}$. They are compared with the noise curves of a few detectors. We extracted the noise curve data from GWplotter (<http://gwplotter.com>) developed by Moore et al. (2015) in which ALIA data is taken from Bender et al. (2013), LISA noise data is from Amaro-Seoane et al. (2012), and TianQin data is from Luo et al. (2016). For DECIGO and BBO noise data we use an analytic expression from Yagi & Seto (2011), while we use an expression from Isoyama et al. (2018) for B-DECIGO. The remnant mass is in the range of $1.17 - 1.27M_\odot$ with the core mass fraction $0.65 - 0.92$. The direction of the sequence to which the model spin up (as measured by the axis ratio) is indicated by an arrow. As the remnant rotationally flattens more, the frequency of the gravitational wave increases and so does the characteristic amplitudes. Near the mass-shedding limit the frequency decreases (as is seen in Fig. 2 the eigenfrequency has its maximum before it reaches the mass-shedding limit) though the amplitude increases. We see DECIGO and BBO will see the mode for the saturation amplitude of $\epsilon_I = \mathcal{O}[10^{-2} - 10^{-1}]$ as is found in Shibata et al. (2002). For this parameter set, TianQin may see the signal if the remnants is close to mass-shedding limit and the amplitude of the mode is

maximal. On the other hand the amplitude suggested by the saturation of Rossby-wave instability may allow the signals to be detected by DECIGO and BBO only for the remnants close to mass-shedding limit.

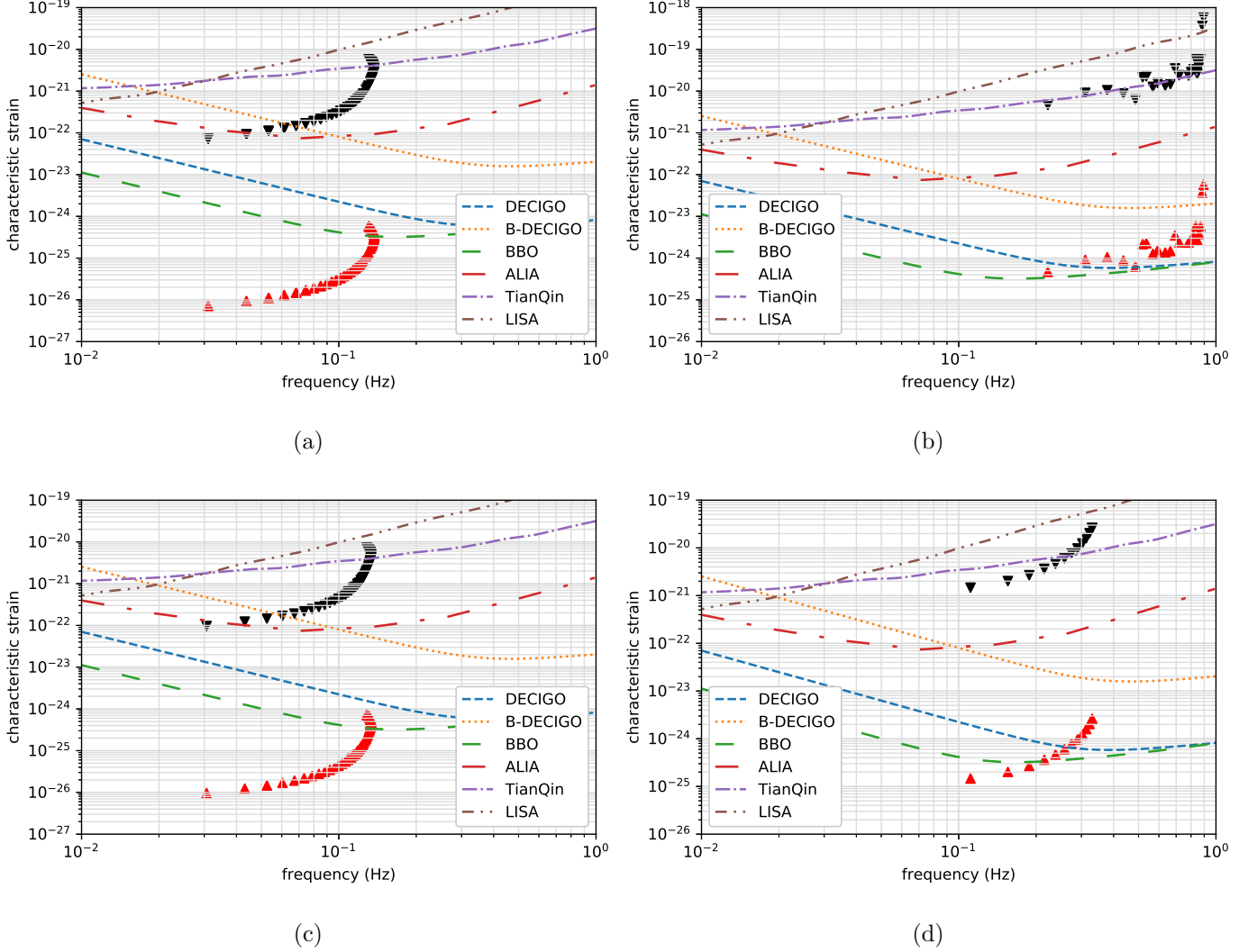


Figure 6. Characteristic strain of GW from unstable oscillations as a function of frequency. (a): $(T_c, \rho_c, \alpha, \beta, R_c) = (10^8, 10^7, 100, 10, 0.4)$. (b): $(T_c, \rho_c, \alpha, \beta, R_c) = (10^8, 10^9, 100, 10, 0.4)$. (c): $(T_c, \rho_c, \alpha, \beta, R_c) = (10^9, 10^7, 100, 10, 0.4)$. (d): $(T_c, \rho_c, \alpha, \beta, R_c) = (10^7, 10^8, 20, 10, 0.4)$.

In Fig.6 the qualitative behavior of the gravitational wave frequency and its strain is similar to Fig.5. For less/more massive stars with the lower/higher central density the frequency and the strain of the gravitational wave are lower/higher (compare panel (a) and (b) with Fig.5). For $\rho = 10^9 \text{ g cm}^{-3}$

even the minimal saturation amplitude models may be detectable by BBO or DECIGO, although the mass range is between $1.35 - 1.42 M_{\odot}$ and the carbon detonation may occur in the early stage of the remnant evolution. Panel (c) is for a higher temperature than in (b) but with smaller ρ_c . Therefore the electron degeneracy is weaker. It increases the strain compared with (a), though the difference is not significant.

For an Ω profile with less gradient at the core-envelope boundary as in panel (b) of Fig.3, the instability becomes weaker in a sense that the range of axis ratio in which instability occurs is smaller and that the growth time scale of the fastest growing eigenmode is longer. Still the characteristic strain for this case may be large enough to be observed (See panel (d). It corresponds to panel (b) of Fig.3).

4. SUMMARY AND DISCUSSIONS

SNeIa have little been considered as sources of GW (see [Falta et al. \(2011\)](#) for a model where SN Ia explosion of non DWD merger origin as a GW source), though their possible progenitor binaries may be observed by the space-borne interferometers. We here consider the possibility of observing merger remnants of DWD by gravitational wave detectors in decihertz band. A merger may leave a rapidly and differentially rotating remnant which have a hot envelope formed through accretion of the secondary star in the progenitor binary onto the primary. The angular velocity profile of the remnant in the early phase of its evolution is expected to have a steep gradient around the core-envelope interface. In these system a dynamical instability is expected which is related to corotation of the oscillation pattern of fluid to the remnant's rotation. We see the fastest growing eigenmode has the nature of inertial oscillation, whose restoring force is the Coriolis force. This is consistent with the recent result of a study in the context of neutron star merger ([Passamonti & Andersson 2020](#)), which is reasonable since the merger process may lead to a similar rotational profile (slowly and uniformly rotating core surrounded by a rapidly rotating envelope). The instability mechanism may not be the same as that in the so-called 'low-T/W' instability found in differentially rotating stars with a monotonic rotational profile, where it is likely that overreflection of acoustic wave at the corotation singularity plays a key role ([Yoshida & Saijo 2017](#)). It may be possible that overrefraction

of the inertial (Rossby) wave at the corotation radius plays a similar role in the current case as in the conventional low-T/W instability.

Saturation of amplitude of the fastest growing modes may sustain quasi-stable quadrupole deformation of the remnant. It may emit gravitational wave at nearly constant frequency, though it only lasts for $10^3 - 10^4$ s in which viscosity smooth out the differential rotation. Therefore we may see a transient gravitational wave signal of nearly constant frequency from an unstable inertial oscillation whose frequency is in decihertz range. The characteristic strain amplitude at Virgo cluster is well above the noise curves of such proposed detectors as BBO or DECIGO, if the density (or mass) and the saturation amplitude is large enough. It may leads to as much as ten observable events per year (See Sec.1). It should be noted that the present mechanism of gravitational radiation works not only in a massive merger that may eventually lead to SNIa, but in a lighter one which survives the thermonuclear runaway. In fact the gravitational wave from a very massive merger may not be observable if it promptly explodes.

As a final remark, we may speculate a prompt mechanism of SNIa related to the unstable oscillations. Relatively massive DWD may survive the initial dynamical accretion phase of its merger and settles down to a quasi-equilibrium state. If it has a sufficient degree of differential rotation, the instability considered here grows. The remnant is like a sound box of trapped inertial/sound wave whose amplitude grows. The density fluctuation at the core-envelope boundary may become large enough to trigger deflagration/detonation wave to travel in the degenerate core, leading to the thermonuclear runaway. If this is the case the explosion is expected to occur during which the gravitational signal considered in the current study is observed. This may be an interesting target of multi-messenger astronomy related to SNIa. It should be noticed that this mechanism is expected to leave a trace of quadrupolar asymmetry in the explosion.

ACKNOWLEDGMENTS

I thank the anonymous reviewer for her/his useful comments to improve the paper. This work is supported by MEXT/JSPS KAKENHI Grant-in-Aid for Scientific Research (C) 18K03641.

REFERENCES

- Abou El-Neaj, Y., Alpigiani, C., Amairi-Pyka, S., et al. 2019, arXiv e-prints, arXiv:1908.00802
- Amaro-Seoane, P., Aoudia, S., Babak, S., et al. 2012, arXiv:1201.3621
- Ando, M., Ishidoshiro, K., Yamamoto, K., et al. 2010, *Phys. Rev. Lett.*, 105, 161101
- Badurina, L., Bentine, E., Blas, D., et al. 2020, *JCAP*, 2020, 011
- Balbus, S. A., & Hawley, J. F. 1991, *ApJ*, 376, 214
- Bender, P. L., Begelman, M. C., & Gair, J. R. 2013, *Classical and Quantum Gravity*, 30, 165017
- Benz, W., Bowers, R. L., Cameron, A. G. W., & Press, W. H. . 1990, *ApJ*, 348, 647
- Blanchet, L., Damour, T., & Schaefer, G. 1990, *MNRAS*, 242, 289
- Centrella, J. M., New, K. C. B., Lowe, L. L., & Brown, J. D. 2001, *ApJL*, 550, L193
- Chandrasekhar, S. 1960, *Proceedings of the National Academy of Science*, 46, 253
- . 1987, *Ellipsoidal figures of equilibrium* (Dover, New York)
- Corvino, G., Rezzolla, L., Bernuzzi, S., De Pietri, R., & Giacomazzo, B. 2010, *Classical and Quantum Gravity*, 27, 114104
- Cox, J. P., & Giuli, R. T. 1968, *Principles of stellar structure*
- Crowder, J., & Cornish, N. J. 2005, *Phys. Rev. D*, 72, 083005
- Dan, M., Rosswog, S., Guillochon, J., & Ramirez-Ruiz, E. 2011, *ApJ*, 737, 89
- . 2012, *MNRAS*, 422, 2417
- Falta, D., Fisher, R., & Khanna, G. 2011, *PhRvL*, 106, 201103
- Ferrario, L., de Martino, D., & Gänsicke, B. T. 2015, *SSRv*, 191, 111
- Graham, P. W., Hogan, J. M., Kasevich, M. A., Rajendran, S., & Romani, R. W. 2017, arXiv e-prints, arXiv:1711.02225
- Hachisu, I. 1986, *ApJS*, 61, 479
- Huang, S.-J., Hu, Y.-M., Korol, V., et al. 2020, *Phys. Rev. D*, 102, 063021
- Iben, I., J., & Tutukov, A. V. 1984, *ApJS*, 54, 335
- Ipsier, J. R., & Lindblom, L. 1991, *ApJ*, 379, 285
- Isoyama, S., Nakano, H., & Nakamura, T. 2018, *Progress of Theoretical and Experimental Physics*, 2018, <https://academic.oup.com/ptep/article-pdf/2018/7/073E01/25332865/pty078.pdf>, 073E01
- Kalogera, V., Narayan, R., Spergel, D. N., & Taylor, J. H. 2001, *ApJ*, 556, 340
- Kashyap, R., Fisher, R., García-Berro, E., et al. 2017, *ApJ*, 840, 16
- Kawamura, S., Nakamura, T., Ando, M., et al. 2006, *Classical and Quantum Gravity*, 23, S125
- Licquia, T. C., & Newman, J. A. 2015, *ApJ*, 806, 96
- Lorén-Aguilar, P., Guerrero, J., Isern, J., Lobo, J. A., & García-Berro, E. 2005, *MNRAS*, 356, 627

- Lorén-Aguilar, P., Isern, J., & García-Berro, E. 2009, *A&A*, 500, 1193
- Lovelace, R. V. E., Turner, L., & Romanova, M. M. 2009, *ApJ*, 701, 225
- Luo, J., Chen, L.-S., Duan, H.-Z., et al. 2016, *Classical and Quantum Gravity*, 33, 035010
- Maoz, D., Hallakoun, N., & Badenes, C. 2018, *MNRAS*, 476, 2584
- Meheut, H., Lovelace, R. V. E., & Lai, D. 2013, *MNRAS*, 430, 1988
- Moore, C. J., Cole, R. H., & Berry, C. P. L. 2015, *Classical and Quantum Gravity*, 32, 015014
- Oohara, K., & Nakamura, T. 1989, *Progress of Theoretical Physics*, 82, 535
- Ostriker, J. P., & Bodenheimer, P. 1973, *ApJ*, 180, 171
- Ostriker, J. P., & Tassoul, J. L. 1969, *ApJ*, 155, 987
- Ou, S., & Tohline, J. E. 2006, *ApJ*, 651, 1068
- Pakmor, R., Kromer, M., Taubenberger, S., et al. 2012, *ApJL*, 747, L10
- Passamonti, A., & Andersson, N. 2015, *MNRAS*, 446, 555
- . 2020, arXiv e-prints, arXiv:2003.10198
- Pickett, B. K., Durisen, R. H., & Davis, G. A. 1996, *ApJ*, 458, 714
- Piro, A. L. 2008, *ApJ*, 679, 616
- Press, W. H., Teukolsky, S. A., Vetterling, W. T., & Flannery, B. P. 1992, *Numerical recipes in FORTRAN. The art of scientific computing*
- Raskin, C., Scannapieco, E., Fryer, C., Rockefeller, G., & Timmes, F. X. 2012, *ApJ*, 746, 62
- Saijo, M., Baumgarte, T. W., & Shapiro, S. L. 2003, *ApJ*, 595, 352
- Saijo, M., & Yoshida, S. 2006, *MNRAS*, 368, 1429
- . 2016, *PhRvD*, 94, 084032
- Sato, Y., Nakasato, N., Tanikawa, A., et al. 2015, *ApJ*, 807, 105
- . 2016, *ApJ*, 821, 67
- Schutz, B. F. 1980, *MNRAS*, 190, 21
- Sedda, M. A., Berry, C. P. L., Jani, K., et al. 2019, *The Missing Link in Gravitational-Wave Astronomy: Discoveries waiting in the decihertz range*, , arXiv:1908.11375
- Segretain, L., Chabrier, G., & Mochkovitch, R. 1997, *ApJ*, 481, 355
- Shakura, N. I., & Sunyaev, R. A. 1973, *A&A*, 500, 33
- Shen, K. J., Bildsten, L., Kasen, D., & Quataert, E. 2012, *ApJ*, 748, 35
- Shibata, M., Karino, S., & Eriguchi, Y. 2002, *MNRAS*, 334, L27
- . 2003, *MNRAS*, 343, 619
- Spruit, H. C. 1999, *A&A*, 349, 189
- . 2002, *A&A*, 381, 923
- Tanikawa, A., Nakasato, N., Sato, Y., et al. 2015, *ApJ*, 807, 40
- Tassoul, J.-L. 1978a, *Theory of rotating stars*
- . 1978b, *Theory of rotating stars*, Chap.10 (Princeton University Press, New Jersey)
- Tassoul, J. L., & Ostriker, J. P. 1968, *ApJ*, 154, 613
- Tayler, R. J. 1973, *MNRAS*, 161, 365

- Velikhov, E. P. 1959, Zhur. Eksptl'. i Teoret. Fiz., 36
- Watts, A. L., Andersson, N., & Jones, D. I. 2005, ApJL, 618, L37
- Webbink, R. F. 1984, ApJ, 277, 355
- Xie, X., Hawke, I., Passamonti, A., & Andersson, N. 2020, PhRvD, 102, 044040
- Yagi, K., & Seto, N. 2011, Phys. Rev. D, 83, 044011
- Yoon, S.-C., Podsiadlowski, P., & Rosswog, S. 2007a, MNRAS, 380, 933
- Yoon, S. C., Podsiadlowski, P., & Rosswog, S. 2007b, MNRAS, 380, 933
- Yoshida, S. 2019, MNRAS, 486, 2982
- Yoshida, S., & Saijo, M. 2017, MNRAS, 466, 600
- Zwerger, T., & Müller, E. 1997, A&A, 320, 209